RSC Sustainability

ROYAL SOCIETY OF CHEMISTRY

PAPER

View Article Online
View Journal | View Issue

Cite this: *RSC Sustainability*, 2023, **1**, 898

Adsorption of sulfate ions from water by $CaCl_2$-modified biochar derived from kelp†

Bingbing Tian, Yalong Song, Rubin Wang, Yi Wang, Tianyang Wang, Jinhui Chu, Zhu Qiao, Min Li, * Jianjiang Lu * and Yanbin Tong

In order to prevent the slow degradation of pristine water ecosystems caused by increasing SO_4^{2-} in natural water bodies (lakes and rivers), innovative and cost-effective remediation techniques are urgently required. Using natural waste kelp trimmings as the carbon source, the $CaCl_2$ activation-carbonation process generates an ecologically acceptable biomass carbon adsorbent. To adsorb SO_4^{2-} from an aqueous solution, kelp-based activated carbon adsorption material (KPC) was created. According to FT-IR research, KPC has many active groups, namely OH and C–O, which further improve adsorption efficiency. The adsorbent had the following property characteristics: The TEM-EDS, XPS, and BET characterization studies were used to describe the adsorbent, and the findings showed that Ca^{2+} was present on the surface of the unactivated kelp-based activated carbon material (UKC). Compared to UKC, KPC has a porous structure and a greater specific surface area. KPC shows good affinity for SO_4^{2-} with a maximum sulfate adsorption capacity of 866.98 mg g^{-1}, which is much higher than that of other materials (such as grapefruit peel (35.21 mg g^{-1} adsorption) and coconut shell (4.90 mg g^{-1} adsorption)). Kinetic studies showed that the adsorption of sulfate ions from simulated water (SW) and Ulungu lake water (LW) followed quasi-secondary kinetics. Isotherm data analysis shows that the Langmuir isotherm model is compatible with SO_4^{2-} in simulated water.

Received 16th December 2022
Accepted 1st April 2023

DOI: 10.1039/d2su00136e

rsc.li/rscsus

Sustainability spotlight

This work reported that natural waste kelp was used as a carbon source to prepare a biochar adsorbent and used for the treatment of SO_4^{2-} in lakes and rivers to protect the aquatic ecosystem environment, meet the national sustainable development strategy, and respond economically, effectively and sustainably. TEM-EDS, XPS, and BET describe the adsorbent characteristics. According to the FT-IR study, KPC has many active groups, further improving adsorption efficiency. In addition, this work is consistent with the United Nations' goal of sustainable consumption and production of chemical products.

1 Introduction

Sulfate (SO_4^{2-}) is ubiquitous not only in heavy-metal polluted effluents but also in natural waters. High concentrations of SO_4^{2-} can cause water mineralization, corrosion and scaling of steel pipes and equipment, damage to mammals, and the generation of poisonous and corrosive H_2S in the sewer system.[1–3] Therefore, many techniques have been applied to reduce and reclaim sulfate ions from wastewater, including adsorption, chemical coagulation, and ion exchange.[4–8] Compared with other methods, adsorption is the most favorable of all contemporary environmental cleanup solutions since it is cost-effective, uses little energy, and is very simple to execute.[9]

Many studies have shown that significant SSA,[10] high pore capacity, and porous carbon can be prepared by pyrolysis and activation of biomass materials with a special plant structure.[11–13] The biomass material precursors for porous carbon can save costs and alleviate the shortage of fossil fuels and environmental pollution. These precursors include the natural waste durian shell,[14] spent mushroom substrate (SMS),[15] hardwood and corn straw,[16] litchi shell, mung bean flour,[17] peanut shell,[18] local forest (tree branches),[19] and so on.[20–24] In contrast, there are few reports on using marine organisms as porous carbon raw materials. Biochar prepared by using *Laminaria japonica* has functional characteristics, and can be directly used as carbon sources and applied in soil remediation in agricultural fields, as a catalyst,[25] catalyst support,[26] and biological adsorbent[27] in the application of wastewater treatment, and also in lithium batteries and sensors.[28] Kelp is one of the most common edible seaweeds, and is an excellent raw material for the preparation of porous carbon because of its low cost, vast source, rapid reproduction, high yield, high

Key Laboratory of Environmental Monitoring and Pollutant Control of Xinjiang Bingtuan, School of Chemistry and Chemical Engineering, Shihezi University, Shihezi, 832000, Xingjiang, China. E-mail: limin@shzu.edu.cn

† Electronic supplementary information (ESI) available. See DOI: https://doi.org/10.1039/d2su00136e

reproducibility, inherent richness in N, P, S and other multiple elements, and its biomass micro-pore channel structure. It should be highlighted that *Laminaria japonica* is grown worldwide, with China's output ranking first, but a significant portion remains mainly unused and will be discarded. As a result, using waste kelp trimmings to make high-performance porous carbon and develop new green energy would yield tremendous economic advantages while also ensuring global sustainability.

Due to the high oxygen-containing functional groups of kelp,[29] kelp adsorption has been extensively documented to remove organic dyes and heavy metal ions from wastewater.[30,31] However, many activated carbons are made in a time-consuming, multi-step, and ecologically unfriendly process. As activators, KOH, HCl, H_2SO_4, $FeCl_3$, $ZnCl_2$, and other chemicals are employed, and these chemicals are eliminated in the succeeding process, which can pollute the environment. As a result, a simple, green, and scalable method for preparing multistage porous biomass carbon employing kelp as the raw material and green chemical activators is urgently needed. Chemical activation of biomass waste with $CaCl_2$ instead of NaOH/KOH/$ZnCl_2$ is an effective method to prepare porous carbon for adsorption. However, studying porous carbon using the $CaCl_2$ chemical activation method has not attracted much interest. Nevertheless, as far as recent studies have shown, calcium chloride-modified biomass carbon is widely used in supercapacitors due to the green color exhibited by the activator and the high pore-forming capacity.[17] There is insufficient research on calcium chloride-modified biomass carbon adsorbent materials compared to that on other adsorbents for pollutants.

The base carbonaceous materials used in the study were wasted kelp. Although the World Health Organization (WHO) guideline for maximum permissible concentration (MPC) for sulfate in drinking water is 250 mg L^{-1}, most previous studies[5] on sulfate removal worked with initial sulfate concentrations that are less than the stated MPC. Also, in practice, real contaminated sources and wastewater contain sulfate concentrations that are often higher than the MPC. Therefore, in this study, a new carbon material of $CaCl_2$ modified with natural waste kelp trimmings was prepared to improve the treatment of sulfate ion wastewater. In this study, the adsorption this study involved (1) characterization of KPC (kelp-based activated carbon adsorption material), UKC (kelp-based activated carbon material), used sample (US), pre-carbonized sample (PCS), and raw sample (RS) so that any changes in surface and chemical species could be recognized; (2) batch adsorption experiments to evaluate the absorption of SO_4^{2-} by KPC, supported by adsorption kinetic and thermodynamic studies. Based on the analysis, our study also aims (3) to clarify if the adsorbent exhibits a broad prospect for application in water pollutant treatment.

2 Experimental section

2.1 Materials

The dried *Laminaria japonica* powder with a particle size of 200 mesh was obtained from Rongcheng Three Penguin E-Commerce Co., Ltd in Shandong Province (China). All other chemical reagents, including hydrochloric acid (37 wt%, HCl, analytical reagent grade) and calcium chloride ($CaCl_2$, analytical reagent grade) were used without further purification. SO_4^{2-} standard solution (1 mg mL^{-1}) was purchased from Shenzhen Chengyuan Technology Co., Ltd (China), and barium chromate ($BaCrO_4$, analytical reagent grade) was purchased from Guangfu Fine Chemical Research Institute, Tianjin, China, and were used without further purification. Deionized (DI) water was used throughout all experiments.

2.2 Preparation of the adsorbent

In this paper, kelp powder was used as a precursor to prepare biomass activated carbon, including by pre-carbonization, activated carbonization, and post treatment. During the pre-carbonization process, kelp powder was dried at 105 °C for 2 hours, and then transferred to a crucible. Then, the crucible was covered, placed in a porcelain boat, and then placed in a muffle furnace for carbonization. After sealing the muffle furnace, a program must be set up to increase the temperature to the predetermined carbonization temperature (300 °C) at a rate of 11 °C min^{-1} at room temperature for 2 hours before it was taken out, and then cooled (cooling rate: 11 °C min^{-1}) to room temperature.

During the activation and carbonization process, the obtained carbide and activator calcium chloride solution (mass concentration 30%) are fully mixed in a 1 : 3 mass ratio, and then placed in a tubular furnace under the protection of a nitrogen gas stream. This was activated for 2 hours, heated at 5 °C min^{-1}, activated at 700 °C, naturally cooled to room temperature, and then removed. First, the activated carbon is washed six times by centrifugation with ethanol. Then the supernatant was poured out, centrifuged with deionized water 6 times, and centrifuged to neutral at 7000 rpm for 6 minutes. Finally, the activator is recovered and filtered, and the filter cake is dried to a constant mass at 105 °C and stored. The schematic diagram of preparing porous carbon from waste kelp excipients.

2.3 Characterization

Morphology and particle size distributions of prepared samples were investigated by scanning electron microscopy (SEM) (JSM 7500F, Japan) and TEM-EDS (FEl Talos F200i). Carbon, hydrogen, nitrogen, and sulfur contents of the samples were determined using a CHN element analyzer (Elementar Vario EL) with a detection limit of 0.1%. In addition, the samples' Fourier transform infrared (FT-IR) spectra were recorded at room temperature according to the KBr.

(Sigma-Aldrich ≥99%) pellet method (sample: KBr = 1 : 100) on a PerkinElmer Spectrum 100 spectrophotometer in the 400–4000 cm^{-1} range with an average of 50 scans. The resolution was better than 4 cm^{-1}. The Brunner–Emmett–Teller (BET) method determined the specific surface areas of adsorbents in an ASAP 2460 with N_2 gas. The BJH (Barret–Joyner–Halenda) method obtained the pore radius distribution from the adsorption branch. The samples were evacuated overnight at 90°C. The zeta potential of the obtained suspension was determined using a Zeta potential analyzer (NanoPIUS-3). The

elemental composition and the chemical bonding state on the sample surface were determined using X-ray photoelectron spectroscopy (XPS) (Thermo Scientific K-Alpha). A curve-fitting program (XPS-Avantage software) was used to fit the XPS results under Shirley's background. The crystallographic structures of the biochars were observed using X-ray diffraction (XRD, Bruker D8 Advance), and the samples were scanned from 5 to 90° with a scan speed of 10° min^{-1}.

2.4 Batch experiments

The adsorption experiment studied the removal of SO_4^{2-} by porous carbon, under the condition that certain experimental conditions remain unchanged, and other experimental factors are carried out according to a low to high gradient for adsorption experiments. The design experiment is shown in Table 1.

The removal efficiencies and the adsorption amount of sulfate on porous carbon were calculated according to the following eqn (1) and (2):

$$q_e = \frac{(C_0 - C_e) \times V}{W} \quad (1)$$

$$\eta = \frac{(C_0 - C_e)}{C_0} \times 100\% \quad (2)$$

where q_e is the equilibrium concentration of sulfate adsorbed on porous carbon, V is the volume of simulated sulfate wastewater (L), C_0(mg L^{-1}) and C_e(mg L^{-1}) are the initial concentration and the equilibrium concentration of SO_4^{2-}, respectively, and W is the mass of the adsorbent (g).

The test was conducted using the barium chromate photometric technique. 0.00 mL, 0.25 mL, 1.00 mL, 2.00 mL, 4.00 mL, 6.00 mL, 8.00 mL, and 10.00 mL of sulphate standard solution, made up to 50 mL with deionized water, were added to eight conical flasks. Each of the eight conical flasks received 1 mL of a 2.5 moL L^{-1} hydrochloric acid solution, which was added, heated, and then maintained at the boiling point for 20 minutes. Once the mixture has cooled a little, 1 + 1 ammonia and 2 drops of ammonia were added to give it a lemon yellow hue. After being progressively filtered using qualitative filter paper using a conical flask that had been well chilled, the filtrate was transferred to a 50 mL volumetric flask, where water was poured to scale. The spectrophotometer's wavelength was adjusted to 420 nm, and a standard curve was plotted after measuring the absorbance using a 10 mm cuvette. Using the aforementioned technique, the sulphate ion concentration of the water samples was also measured. Every time, 50 mL of the water sample to be analyzed was taken, its absorbance was determined using the aforementioned procedure, and its sulfate ion concentration was calculated using the standard curve.

Table 1 Single factor experimental factor level

Serial number	Investigating factors	Level
1	Dose/g	0.1–0.5
2	Concentration of SO_4^{2-}/(g L^{-1})	0.3–0.9
3	pH	5.0–9.0
4	Adsorption time/min	30–150
5	T/°C	25–50
6	Rotating speed/rpm	100–165

2.5 Adsorption kinetics and thermodynamics studies

2.5.1 Adsorption isotherm models. When the solution concentration is low, the adsorbed SO_4^{2-} does not saturate the adsorption sites on the KPC surface, and the unit adsorption amount is not high; when the solution concentration continues to increase, the unit adsorption amount continues to increase, and when the adsorption sites are close to saturation, the adsorption amount does not increase significantly when the solution concentration increases. In static adsorption experiments, Langmuir, Freundlich, Langmuir–Freundlich, Temkin, and Dubinin–Radushkevich (D–R) equations are often used for the nonlinear fitting of isothermal adsorption data. In this study, the above equations were used to describe and discuss the adsorption behavior of the adsorbent KPC on SO_4^{2-}.

(1) Langmuir model

Under the assumption of the Langmuir isothermal adsorption model, the adsorption sites are uniformly distributed on the adsorbent surface, and the adsorbent and adsorbate have no interaction with each other, which is a single molecular layer adsorption. The nonlinear and linear expressions of the Langmuir isothermal model:[32]

$$\text{Nonlinear}: \ q_e = \frac{K_L q_m C_e}{1 + K_L C_e} \quad (3)$$

$$\text{Linear}: \ \frac{C_e}{q_e} = \frac{1}{K_L q_m} + \frac{C_e}{q_m} \quad (4)$$

The essential features of the Langmuir isothermal adsorption model will be described by the equilibrium constant (R_L), which determines the affinity between the adsorbent and the adsorbate, expressed as eqn (5):

$$R_L = \frac{1}{1 + K_L C_0} \quad (5)$$

where C_0 is the initial concentration of the solution (mg L^{-1}), $R_L = 0$ for irreversible adsorption, $0 < R_L < 1$ for favorable adsorption, $R_L = 1$ for linear adsorption, and $R_L > 1$ for unfavorable adsorption.

(2) Freundlich isothermal adsorption model

Under the assumption of the Freundlich isothermal adsorption model, the adsorption sites are non-homogeneously distributed on the adsorbent surface, and the adsorbent and adsorbent belong to multilayer adsorption. The linear and nonlinear expressions of the Freundlich isothermal model as eqn (6) and (7):

$$\text{Nonlinear}: \ q_e = K_F C_e^{\frac{1}{n}} \quad (6)$$

$$\text{Linear}: \ \lg q_e = \frac{1}{n} \lg C_e + \lg K_F \quad (7)$$

(3) Langmuir–Freundlich model

$$q_e = \frac{q_m K_{L-F} C_e^{\,n}}{1 + K_{L-F} C_e^{\,n}} \quad (8)$$

(4) The Temkin model has been applied in the following form:[31]

$$q_e = a + b\ln(C_e) \quad (9)$$

(5) D–R model

$$\ln q_e = \ln q_m - \beta\varepsilon^2 \quad (10)$$

where q_e-equilibrium adsorption of sulfate ions by KPC (mg g^{-1}), q_m-maximum adsorption of sulfate ions by KPC (mg g^{-1}), C_e-the concentration of sulfate ions remaining in the solution after adsorption equilibrium (mg L^{-1}), b-constant related to adsorption energy, K_F-Freundlich's constant, $1/n$-uneven factors, K_{L-F}-Langmuir–Freundlich's constant, a, b, and n are constants related to the heat of adsorption; $ß$ is a constant related to the free energy of adsorption; ε is the Polanyi potential energy, and $\varepsilon = RT\ln(1 + 1/C_e)$, where R is the molar constant of the ideal gas, 8.314 J $(\text{mol K})^{-1}$, and T is the absolute temperature (K).

The average free energy of adsorption (4.88 kJ mol^{-1}) can be calculated from the constant $ß$ of the D–R equation[33] (kJ mol^{-1}). The formula is shown in eqn (11).

$$E = \frac{1}{\sqrt{2\beta}} \quad (11)$$

where the E value can determine the type of adsorption reaction, and if $E < 8$ kJ mol^{-1}, it is physical adsorption, if 8 kJ $mol^{-1} < E <$ 16 kJ mol^{-1}, it is ion exchange adsorption, and if $E > 16$ kJ mol^{-1}, it is chemisorption.[34]

2.5.2 Adsorption kinetic models. In the adsorption process, after a certain period, the adsorbent no longer adsorbs SO_4^{2-} and the adsorption reaches saturation, which requires timely replacement of the adsorbent. Therefore, we examined the effect of time on the adsorption performance of KPC to determine when to replace the adsorbent. The specific conditions are shown in Table 2.

After studying the effect of time on adsorption, kinetics is often used to evaluate the entire adsorption process. Kinetics can provide information such as the adsorption rate, which can give an idea of the time required for adsorption. In order to explore the adsorption mechanism in the adsorption process, the experimental kinetic data were fitted using pseudo-first order kinetics, pseudo-second order kinetics, the Elovich model, and the intraparticle diffusion (W–M) kinetic model, and each kinetic equation is shown in eqn (12–15), respectively.[13]

(1) Pseudo-first order kinetics

$$\ln(q_e - q_t) = \ln q_e - k_1 t \quad (12)$$

(2) Pseudo-second order kinetics

$$\frac{1}{q_t} = \frac{1}{k_2 q_e^{\,2}} + \frac{t}{q_e} \quad (13)$$

(3) Intraparticle diffusion (W–M) kinetic model

$$q_t = k_3 \times t^{1/2} + c \quad (14)$$

(4) Elovich model

$$q_t = \frac{1}{a}\ln(bt) \quad (15)$$

where q_t and q_e are the adsorption amount and equilibrium adsorption amount of KPC at time t (mg g^{-1}), k_1 is pseudo-first order kinetics rate parameter (h^{-1}), k_2 is pseudo-second order kinetics rate parameter [g (mg h)$^{-1}$], k_3 is the intraparticle diffusion (W–M) kinetic model, [mg (g $h^{1/2})^{-1}$], and a, b and c are the relevant constants for the Elovich and W–M kinetic equations, respectively.

2.5.3 Thermodynamic parameters. According to the above experiments, by using the relationship between the thermodynamic equilibrium constants (K_0) and the reaction Gibbs free energy ($\Delta G°$), the enthalpy change ($\Delta H°$) and entropy change ($\Delta S°$), the thermodynamic constants for the adsorption reaction of SO_4^{2-} on KPC can be calculated to provide some basis for the thermodynamic properties and reaction process of SO_4^{2-} adsorption by this adsorbent. The specific conditions are shown in Table 3.

The thermodynamic parameters of sulfate adsorption by KPC can be calculated according to eqn (16), (17), and (18).

$$\Delta G^\circ = -RT\ln b \quad (16)$$

$$\Delta G^\circ = \Delta H^\circ - T\Delta S^\circ \quad (17)$$

Table 2 Conditions affecting the temperature in adsorption experiments

Adsorbent	SO_4^{2-}concentration (g L^{-1})	Time (min)	Same experimental conditions
KPC	0.9	30, 60, 90, 120, 150, 180, 240, 300, 360, 420, 480, and 540	pH = 8.0, 0.1 g, 1 h, 120 rpm

Table 3 Conditions affecting the temperature in adsorption experiments

Adsorbent	T (K)	SO_4^{2-}concentration (g L^{-1})	Same experimental conditions
KPC	303.15, 313.15, and 323.15	0.3, 0.5, 0.7, 0.9, 1, 1.2, 1.4, 1.6, 1.8, 2.0, 2.3, 2.6, and 2.9	pH = 8.0, 0.1 g, 1 h, 120 rpm

$$\ln b = \frac{\Delta H^0}{R} - \frac{\Delta H^0}{RT} \quad (18)$$

where T-the temperature in Kelvin, K; R-the universal gas constant, 8.3141 10^{-3} kJ (mol^{-1} K^{-1}); ΔS°-entropy change, J (mol^{-1} K^{-1}); ΔH°-enthalpy change, kJ mol^{-1}; ΔG°-Gibbs free energy, kJ mol^{-1}; b-adsorption isotherm constant, $b = K_L \cdot Q_m$.

3 Results and discussion

The SEM images of different materials at different magnifications are shown in Fig. 1. From Fig. 1a and k, it can be seen that the surface of the pyrolyzed biomass carbon materials (PCS and UKC) was rough and showed a large number of lamellar or reticulated structures compared to that of the original kelp powder (RS), which may be due to the collapse of the biocarbon structure during the release of a large amount of gas produced by the RS during the pyrolysis process.[5] During the preparation of KPC, $CaCl_2$ was loaded onto the kelp surface for modification. The pristine kelp surface is rough after high-temperature pyrolysis, thus forming a porous structure with a large surface area (Fig. 1f). A large number of folds on the surface of carbon fiber facilitates the bonding of calcium ions. It can be observed that the formed $CaCl_2$ agglomerates are tightly attached to the surface of kelp carbon fibers in the form of solids (Fig. 1e and 2b). Moreover, the addition of $CaCl_2$ did not disrupt the folded morphology and porous structure of UKC (Fig. 1b, h, j, d–f and i). The layered porous structure dramatically increases the adsorption sites of sulfate ions in water. At the same time, the formation of not only micro-nano channels on the biomass fibers but also the mutual formation of a macroporous structure, which facilitates the mass transfer of SO_4^{2-} to KPC, further improves the adsorption performance of KPC. Specifically, it can be seen that both the KPC and UKC samples show irregular lumps and a compact network structure. After chemical activation by $CaCl_2$, the carbon particles were oxidized and swollen to form a rough and fluffy structure.

To confirm the role of $CaCl_2$ in this activation thermal cracking process, the same tests were performed on two blank samples of UKC. The internal structure of the $CaCl_2$-activated samples can be further observed by using TEM-EDS images, as shown in Fig. 2. The material is peeled, curled, and stretched during the carbonization process as a disordered lamellar structure (*e.g.*, Fig. 2a).The $CaCl_2$ activation process causes the carbon particles to oxidize and swell, peel off from the carbon layer surface and fold and bend (as in Fig. 2b). Previous studies have pointed out that $CaCl_2$ can react with C to form $CaCO_3$ during the high-temperature carbonization process. After the process, the remaining $CaCO_3$ in the material is washed away with acid and deionized water, and abundant micropores and mesopores emerge.[35] In general, an increase in surface roughness leads to an increase in the specific surface area of the adsorbent, in theory increasing the adsorption efficiency. Therefore, this observation infers that hybrid biosorbents with a high specific surface area may be suitable for ion adsorption processes. In addition, ion exchange may be one of the adsorption mechanisms.

FT-IR spectra were evaluated for raw kelp powder and pre-carbonized kelp powder, and activated-carbonized kelp powder

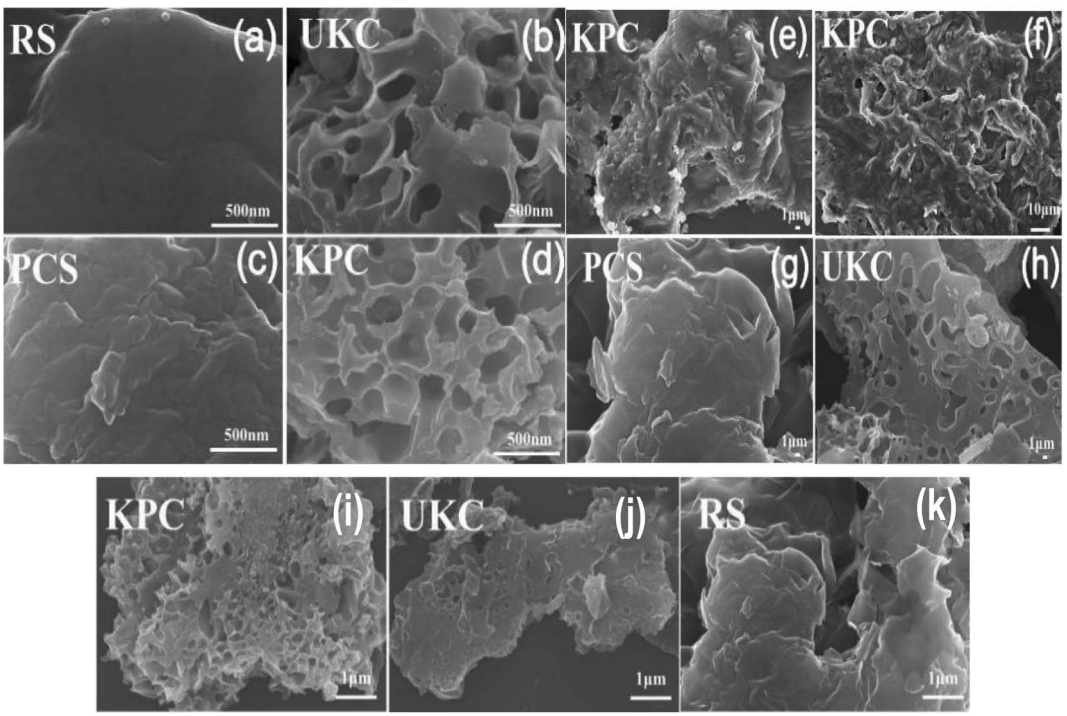

Fig. 1 (c and g) SEM images of the PCS sample, (b, h and j) SEM images of the UKC sample, (d–f and i) SEM images of the KPC sample, (a and k) SEM images of the RS sample at different magnifications.

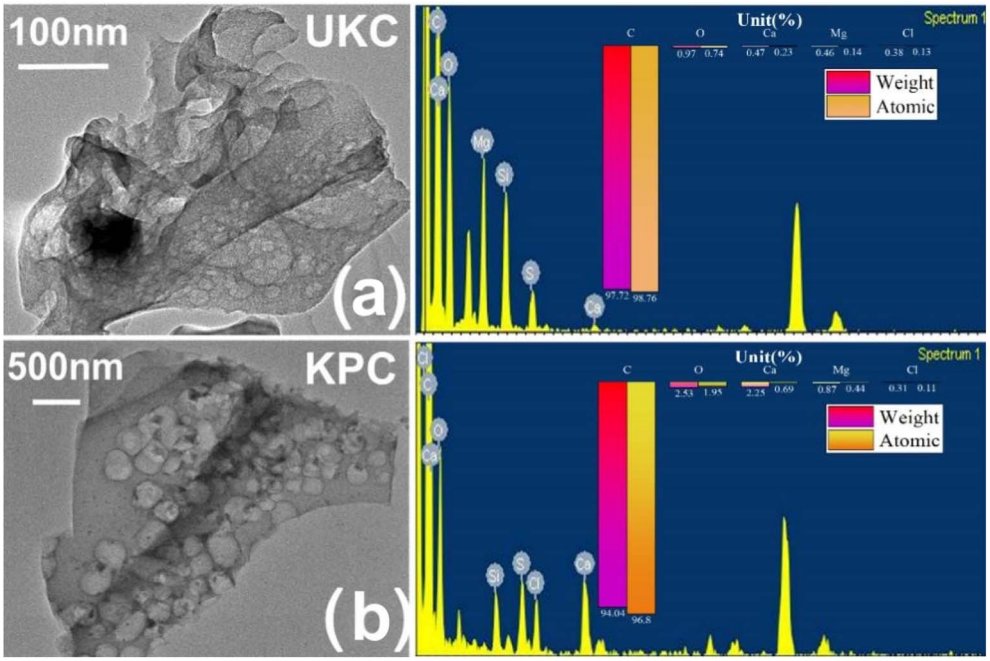

Fig. 2 (a) TEM-EDS images of kelp biochar produced by direct pyrolysis; (b) TEM-EDS plots of kelp biochar produced by the activation method.

in order to confirm the presence of various surface functional groups. The peaks close to 3100 and 3400 cm^{-1} resulting from activated biochars express O–H elongations in Fig. 3(RS) that represent phenols, alcohols, carboxyls, as well as the intrinsic moisture (including interlaminar –OH and interlaminar water molecules –OH) of the materials, and this is consistent with the article reported by Almeida and Liu.[36,37] On the spectrum (PCS and KPC), peaks are found in this interval with intensity changes, signaling that the –OH group has changed after calcination. The peaks close to 2921 and 2926 cm^{-1} represent CH_2 due to the long chains of the raw sample (RS). As the pyrolysis temperature increased, this peak in biochars eventually decreased.[38] Carboxylic acid salts and the amide band have maxima at 1200^{-1} and 1850 cm^{-1}. C–O bonds, which represent alcohols, esters, ethers, and phenols, had peaks ranging from 1029^{-1} to 1250 cm^{-1}.

The number of oxygen-containing functional groups on the surface of biomass carbon materials changes with the pyrolysis

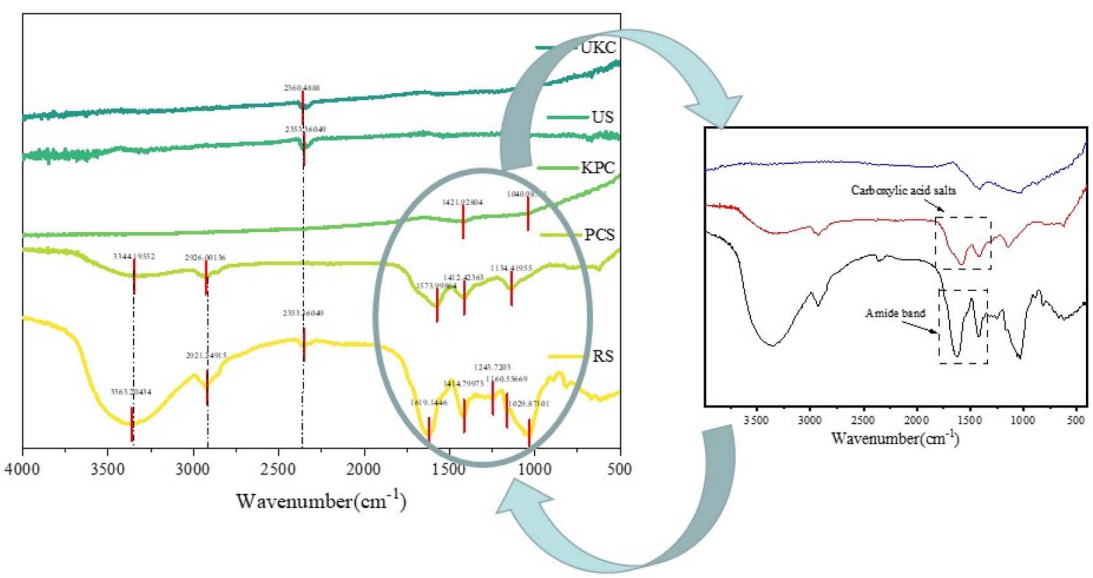

Fig. 3 FT-IR spectra of the raw sample (RS), pre-carbonized sample (PCS) and kelp-based activated carbon adsorption material (KPC), unactivated kelp carbon material (UKC), and used sample (US).

temperature, and the number of surface functional groups changes with the pyrolysis temperature. Recent research has revealed that the carboxyl group in the oxygen-containing functional group is a critical element of biochar characterization.[35] The cellulose in the biomass is transformed into carboxyl groups or esters, which are oxygen-containing functional groups on the surface, during the pyrolysis process. Since the carboxyl group is the active site for adsorbing contaminants, it is crucial to determine the adequate pyrolysis temperature for many oxygen-containing functional groups. The peaks of oxygen-containing functional groups of kelp adsorbing carbon materials strongly appear after pyrolysis, which may help to adsorb pollutants.

The crystal structures of the obtained sample were analyzed by XRD as shown in Fig. 4. After adding calcium chloride to PCS, the KPC sample showed a large number of sharp diffraction peaks, and it is worth mentioning that the diffraction angles 29.34°and 31.33°are consistent with the distinctive peaks of $CaCl_2$. The information related to the carbon morphology in the material was characterized using XRD. All samples have the characteristic peak $2\theta = 25°$, representing the graphic stacking structure (002) surface. $2\theta = 45°$ represents a disordered amorphous carbon stacking (100) surface.[36] The peak intensity of KPC at low angles is higher than that of PCS, indicating a greater density of micropores and a disordered structure, which can provide more active sites for applying adsorbed pollutants. The XRD pattern shows that the material prepared in this experiment mainly contains a large amount of amorphous carbon. It can be observed from the figure that the (002) crystal plane diffraction peaks from PCS to KPC become weaker as the temperature increases, demonstrating an increase in the disorder of the carbon structure. The mixed precursor before the addition of $CaCl_2$ to PCS has no apparent XRD diffraction peak crystalline structure because of the absence of highly dispersed and filled $CaCl_2$ in the biological skeleton. During the thermal cracking and warming process, the high carbonization temperature leads to the collapse of the carbon layer. The biomass carbon with excess oxygen becomes CO_2, which forms calcium carbonate and sodium chloride with calcium and sodium ions and simultaneously reacts with the carbon material to insert heteroatoms into the carbon layer, during which chemical activation and physical activation take place. The highly dispersed $CaCl_2$ aggregates and precipitates to form the crystalline structure $CaCl_2$ The honeycomb structure of carbon materials.

In order to gain insight into the porous structures of the samples, the N_2 adsorption–desorption test was carried out with the isotherms and BJH pore size distribution curves shown in Fig. 5. The BET-specific surface areas (SSA) and porous structure parameters are summarized in Table 4. Based on the IUPAC classification, the isotherms of both UKC and KPC conform to a type IV isotherm for an H_4 type hysteresis loop, representing a typical macroporous structure, with a SSA of only 254.675 $m^2 g^{-1}$. The specific surface area of KPC is smaller than that of UKC, whereas the total pore volume and average pore radius of KPC are higher than that of UKC. This result indicates that the increase of $CaCl_2$ after pre-carbonation promotes the formation of a mesoporous structure. In addition, the pore structure of KPC may collapse and $CaCl_2$ occupies the carbon layer exhibiting defects and inserts in the carbon layer, leading to the blockage of pores, which leads to the reduction of the surface area of KPC. These phenomena are consistent with the results observed by SEM and TEM-EDS. The pore sizes of the two samples were mainly concentrated in the range of 20–40 nm with large pore volumes, which is consistent with the results of N_2 adsorption–desorption isotherm analysis. KPC and UKC exhibited significant capillary coalescence and hysteresis loops in the medium pressure $0.3 < P/P_0 < 0.8$ and high-pressure $P/P_0 > 0.9$ ranges, strongly confirming that $CaCl_2$ activates the carbon materials to build mesopores. Comparing the adsorption isotherms of these two samples, the samples KPC and UKC have

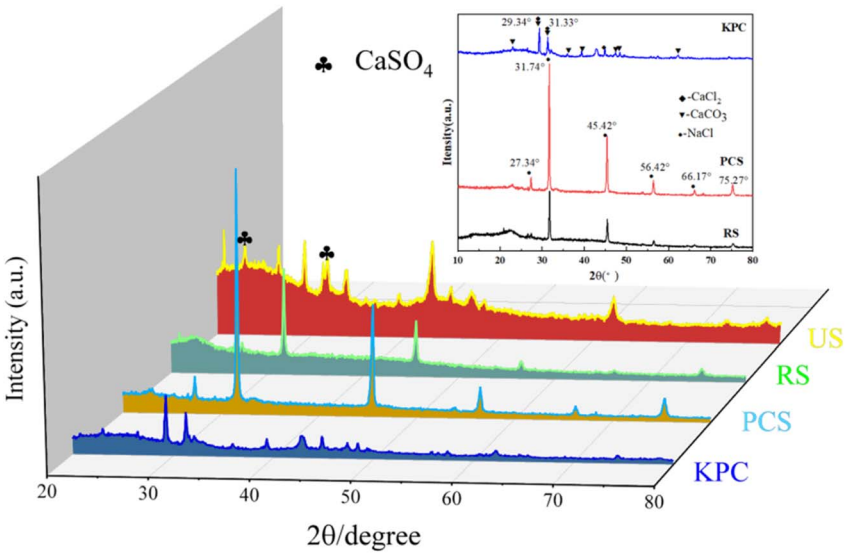

Fig. 4 XRD patterns of the raw sample (RS), pre-carbonized sample (PCS), kelp-based activated carbon adsorption material (KPC), and used sample (US).

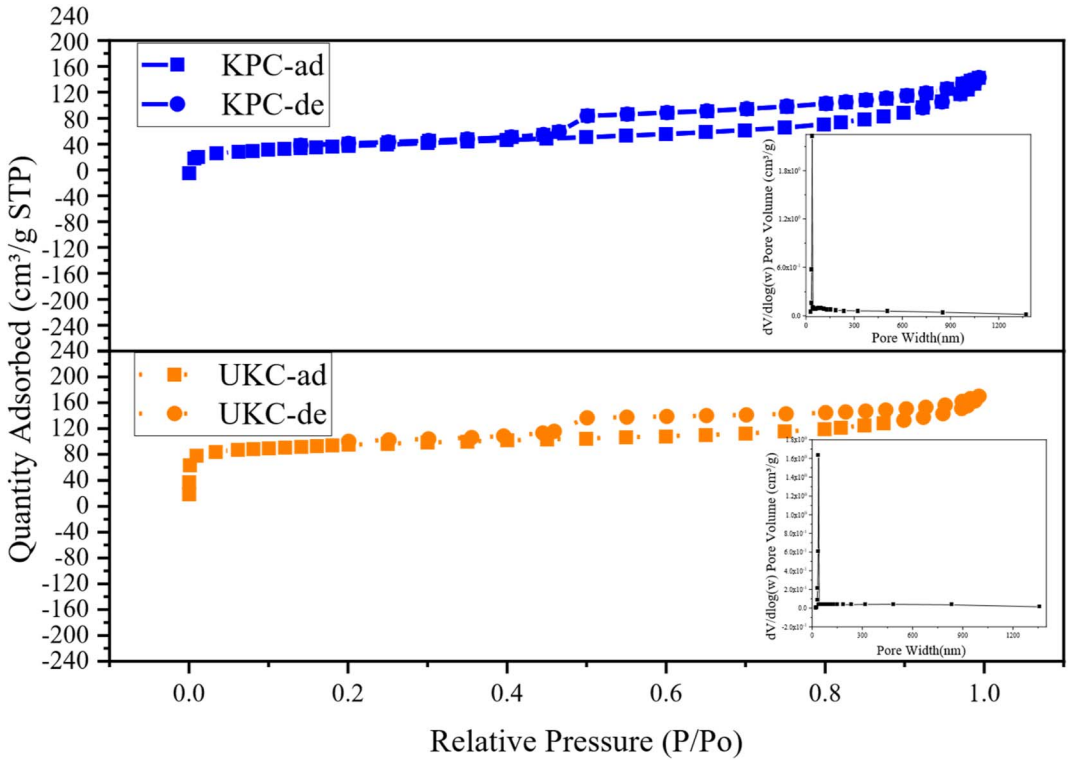

Fig. 5 N_2 adsorption–desorption isotherms and the pore size distributions of the UKC and KPC.

Table 4 Physico–chemical properties of the raw sample (RS), kelp-derived carbon material (KPC), and unactivated kelp-carbon material (UKC)[a]

Parameter	Unit	RS	KPC	UKC	US
C	%	3.12	57.28	60.29	56.82
H	%	5.04	1.38	1.32	1.44
N	%	2.32	2.27	3.09	2.14
S	%	1.23	0.13	0.10	2.81
BET surface area	$m^2\ g^{-1}$	—	254.675	305.8638	—
Pore volume	$cm^2\ g^{-1}$	—	0.281646	0.261817	—
Average pore diameter	Nm	—	44.236	34.240	—

[a] Note: "—" represents ND.

similar adsorption capacities at low relative pressures, implying the presence of more micropores in these two materials. The above test results of these two samples further confirm that $CaCl_2$ is a very effective activation reagent for the preparation of multistage pore carbon materials in this experimental system, which can be influential for pore formation, especially mesopores and macropores. Therefore, it can be used as a green and novel porogenic agent.

Based on comparison with UKC, Ca^{2+} was successfully loaded on the surface of KPC (Fig. 6a), which follows the analysis results of SEM/TEMEDS. The modified kelp showed a decrease in the proportion of C elements and an increase in the proportion of O elements on its surface, possibly due to the loading of calcium oxides on the KPC surface. The weak peak found at 162.79 eV (Fig. 6b) was assigned to the S 2p spectrum, which confirms the adsorption of SO_4^{2-} on the KPC surface. Fig. 6c shows the Ca 2p orbital energy spectra of KPC, and three peaks were obtained after peak splitting, corresponding to Ca 2p1, Ca 2p3, and Ca CO_3 electron orbitals, respectively. 0.97 eV and 1.15 eV, which are due to the loss of Ca electron density due to the binding of KPC with SO_4^{2-}, in turn change the binding energy of Ca 2p1 and Ca 2p3. The elemental carbon content in the UKC sample reached 80.84%, indicating the high yield of porous carbon in kelp. Fig. 6a shows the characteristic peaks of C 1s, O 1s, N 1s, Ca 2p, and S 2p of the samples. The stronger peaks of C 1s and N 1s appear at 284.96 eV and 400.25 eV, respectively, and the weaker peak of O 1s appears at 532.41 eV. The results of the C1s splitting fit (Fig. 6d and e) show the results of the C 1s splitting for the three samples, where the signal peak at 284.8 eV corresponds to the C–C bond, the signal peak at 286 eV corresponds to the C–O–C bond, and the signal peak at 288.5 eV corresponds to the O–C=O bond. The signal peak at 532.5 eV corresponds to an alcohol, phenol, fatty ether, or another hydroxyl-containing compound (COH).[39] These abundant functional groups can improve some properties of the material and increase the activity of KPC. The results of N elemental analysis of the KPC sample are shown in Table 5 above, with 2.27% for elemental analysis and 2.91% for XPS analysis. Such a high nitrogen content indicates that the one-step activation of $CaCl_2$ for heteroatom doping of kelp is simple and effective. This result is consistent with preparing a nitrogen-doped carbon material with an interpenetrating network structure by one-step activation of $CaCl_2$, as reported by Yang *et al.*[32]

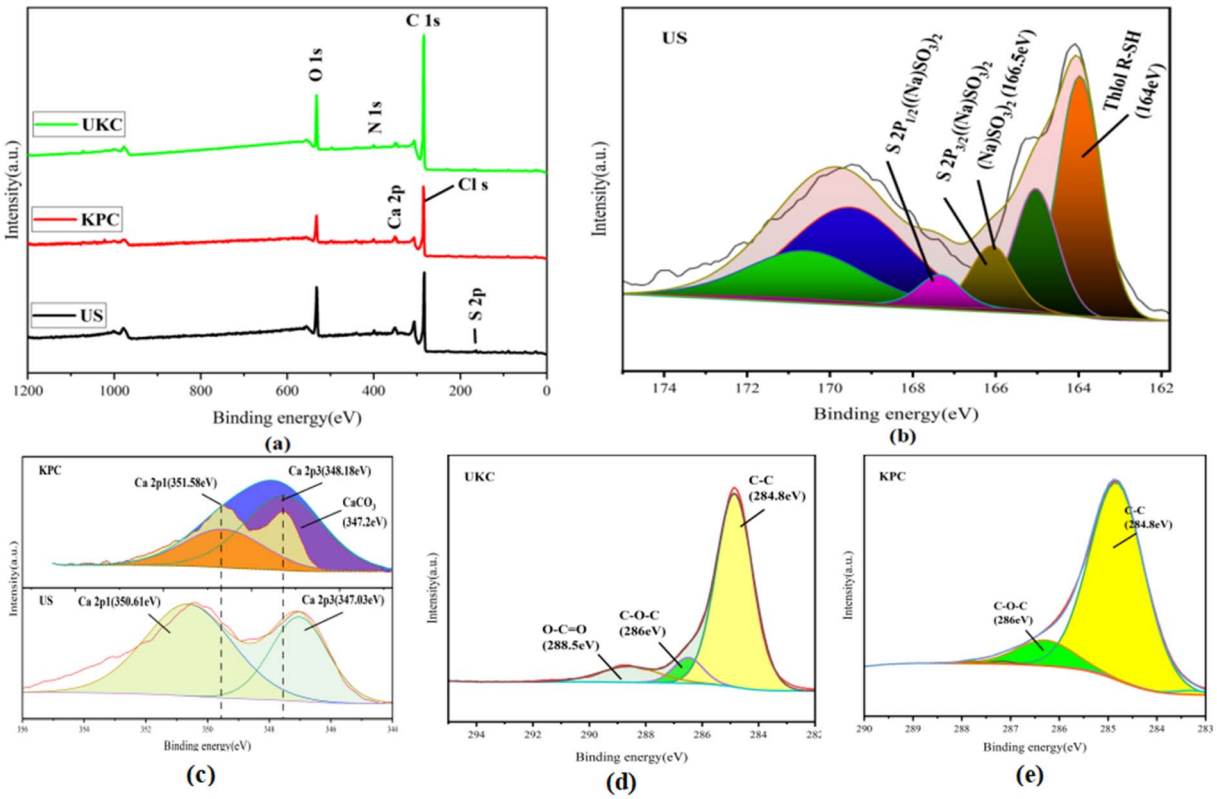

Fig. 6 XPS spectra of UKC, KPC, and post-sorption US: (a) full-spectrum scanning; (b) S 2p orbital spectrum for post-sorption US; (c) Ca 2p1 and Ca 2p3 orbital and (d) C 1s orbital spectra for UKC and KPC.

Table 5 Surface element content of UKC, KPC, and US

	Atomic (%)				
	C	O	Ca	S	N
Biochar UKC	80.84	13.98	0.07	0.98	1.60
KPC	60.56	11.76	2.16	1.28	2.91
US	68.33	20.36	2.70	1.59	4.01

3.2 Batch experiments

The experimental results of adsorption of SO_4^{2-} in simulated water (SW) and lake water (LW). The adsorption experiment employed a variable-controlling approach to explore the factors that influenced the adsorption process, including pH, temperature, adsorbent dosage, and contact time.

3.2.1 Effect of pH on the adsorption of sulfate on KPC. It is necessary to study the adsorption capacity of the adsorbent at different pH values because the pH value change affects the adsorbent's surface charge. pH values varying from 5 to 9 are shown in Fig. 7a. The best adsorption effect of KPC on SO_4^{2-} in simulated water was achieved at solution pH = 5.0. This material had an adsorption amount of 697.62 mg g^{-1}, and the concentration of SO_4^{2-} in the lake water was reduced from 826.53 mg L^{-1} to 17.09 mg L^{-1} under the same conditions. At alkaline pH, negatively charged ions dominate. The ions compete with the sulfate ions for the sorption binding sites on the surface of the KPC, leading to reduced sulfate sorption.

The relevant literature shows that when pH < pH_{PZC}, the charged surface is positively charged; when pH > pH_{PZC}, the charged surface is negatively charged[5] (Fig. 7b). So the reason is analyzed as follows: under acidic conditions, protonation makes the adsorbent surface positively charged, and the reaction follows $CaCl_2 + H_2O + SO_4^{2-} \rightarrow CaSO_4 + Cl^- + OH^-$; thus electrostatic gravitational force and ion exchange make the sulfate ion adsorbed on the adsorbent surface while the solution is alkaline. In addition, the presence of a large number of hydroxide ions (OH^-) in the solution at higher pH values, where OH^- and SO_4^{2-} compete together for the active adsorption sites on the KPC surface, also leads to a decrease in the adsorption capacity of KPC, which precisely explains the rapid decrease in SO_4^{2-} adsorption with increasing pH.

3.2.2 Effect of the initial sulfate concentration on the adsorption of sulfate on KPC. The adsorption capacity of KPC on sulfate ions is shown in Fig. 8. The initial concentration of sulfate solution increased from 0.3 g L^{-1} to 2.9 g L^{-1}, with the adsorption capacity increasing first and then stabilizing. When the initial concentration of SO_4^{2-} was below 900 mg L^{-1}, the adsorption capacity increased rapidly with the increase of SO_4^{2-}. This effect was due to the increase of the driving force formed by the concentration gradient, which increased the chance of mutual collision between the adsorbent and the adsorbent increase, and the adsorption capacity increased.

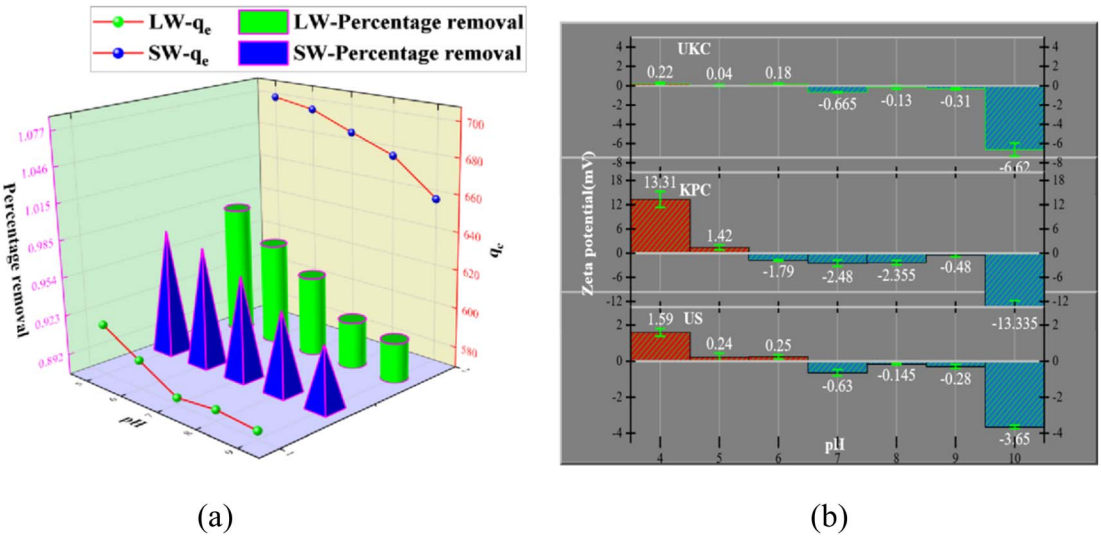

Fig. 7 Effect of pH on SO_4^{2-} adsorption and effect of pH (a) on the zeta potential of UKC, KPC, and US (b).

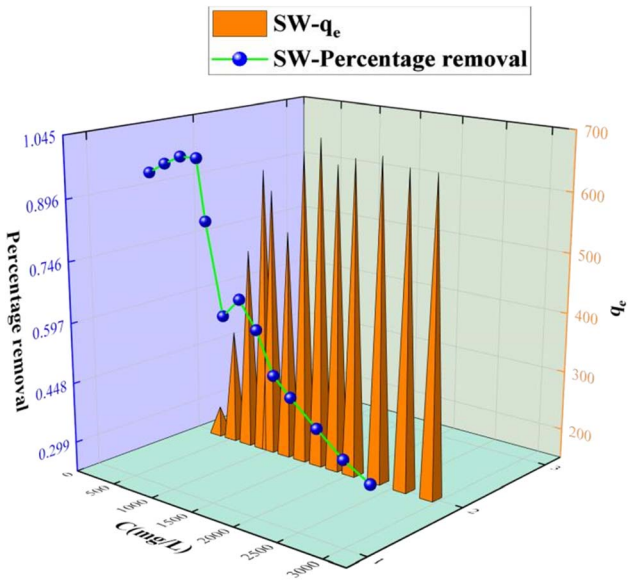

Fig. 8 Effect of the initial sulfate concentration on SO_4^{2-} adsorption.

However, with the further increase of the initial concentration of SO_4^{2-}, the adsorption sites of the adsorbent would decrease with the adsorption process. However, as the initial concentration of SO_4^{2-} increases further, the adsorption becomes saturated.

3.2.3 Effect of dosage on the adsorption of sulfate on KPC. The experimental results of the adsorption of sulfate ions in simulated water and lake water at pH = 8.0, the adsorbent concentration of 500 mg L^{-1}, the temperature of 40 °C, speed of 120 rpm, and contact time of 60 min with different doses of KPC are shown in Fig. 9. The adsorption of sulfate ions increased from 82% to 97% when the amount of KPC was increased from 0.1 g to 0.5 g. Moreover, the adsorption amount decreased with the increase in the dosage. This result may be because when the amount of KPC is small, the active sites on the surface are fully utilized, and the adsorption of sulfate ions per unit mass of KPC is more significant.[2] As the dosage increases, the number of active sites on the surface of KPC increases, and more sulfate ions are adsorbed; thus, the removal rate keeps increasing. On the other hand, the increase in dosage increased the chance of collision between KPC particles, which made the coalescence between particles easier and caused the decrease of total specific surface area and the decrease of adsorption of sulfate ions per unit mass of KPC. From the results of the KPC treatment of lake water, it can be seen that the amount of KPC adsorbent significantly affects the removal capacity of sulfate. As the amount of adsorbent increased, the removal rate gradually increased, and the adsorption capacity gradually decreased. This result may be because adsorption sites cannot

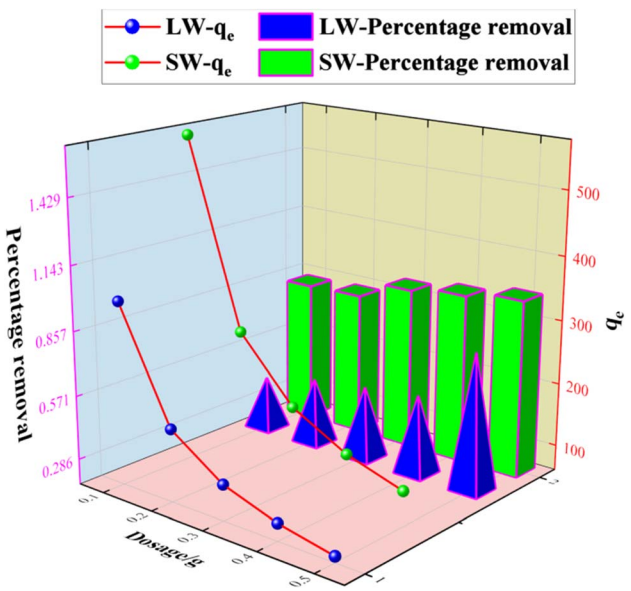

Fig. 9 Effect of dosage on SO_4^{2-} adsorption.

be available on account of saturation and a decrease in the number of dyes adsorbed per unit weight of adsorbent, resulting in a decrease in the utilization of the active center. When KPC reached 0.5 g, the removal rate of sulfate in natural water reached 60%, which means that the residual sulfate concentration in natural water was 165 mg L^{-1}, and this value was far below the requirements of the Sanitary Standard for Drinking Water (GB5749-2006).

3.2.4 Effect of temperature on the adsorption of sulfate on KPC. 0.1 g of KPC adsorbent was accurately weighed in a 250 mL conical flask and added to a simulated sulfate solution with an initial concentration of 900 mg L^{-1}. The system was shaken at 120 rpm at a pH of 8 for 120 min. The effect of adsorption temperatures 25 °C, 30 °C, 35 °C, 40 °C, and 50 °C on the amount of sulfate adsorption was examined. As shown in Fig. 10, the adsorption amount decreased when the temperature was greater than 40 °C, indicating that an appropriate increase in temperature was beneficial for the removal of SO_4^{2-}. However, the overall trend of the residual SO_4^{2-} in the solution at temperatures greater than 25 °C was not particularly obvious, indicating that the effect of reaction temperature on the removal of sulfate was relatively small. Therefore, 25 °C or natural temperature was chosen as the optimum adsorption reaction temperature for the adsorption process.

3.2.5 Effect of the speed rate on the adsorption of sulfate on KPC. Since the stirring speed affects the contact and interaction between the active center of the adsorbent and the adsorbent mass ions, it is essential to evaluate the effect of stirring speed during the adsorption of contaminants. Therefore, the optimal stirring speed during the adsorption of sulfate ions using KPC was determined. 0.1 g of KPC adsorbent was weighed accurately in a 250 mL conical flask and added to 900 mg L^{-1} simulated SO_4^{2-} solution, respectively. The speed rate was adjusted to 100, 120, 135, 150, and 165 rpm, and the mixture was shaken for 60 min to investigate the effect of shaking speed on the adsorption performance of KPC sugar for SO_4^{2-} adsorption. The results are shown in Fig. 11. In the present study, the optimum shaking speed for the adsorption performance of KPC was 120 rpm at 627.46 mg g^{-1}. After that, at 135–165 rpm, the adsorption of sulfate ions from simulated water and lake water decreased sharply from 627.00 mg g^{-1} to 620.34 mg g^{-1} and to 599.20 mg g^{-1}, respectively. At lower shaking speeds, the molecules of sulfate ions (adsorbates) did not have sufficient contact with the binding sites on the KPC. In contrast, the molecules moved too fast at higher shaking speeds and missed the binding sites, leading to decreased adsorption performance. Although the difference in adsorption capacity is insignificant, it is essential to adjust the oscillation speed to about 120 rpm for optimal performance of the KPC for sulfate removal.

3.2.6 Effect of contact time on the adsorption of sulfate on KPC. The adsorbent was accurately weighed (0.1 g) and added to the simulated SO_4^{2-} solution at an initial concentration of 900 mg L^{-1}. The adsorption temperature was determined to be 40 °C, the oscillation speed was 120 rpm, and the system's pH was 8.0. Samples were taken at certain time intervals to determine the sulfate concentration in the clear solution and calculate the adsorption amount of sulfate. The results are shown in Fig. 12.

As can be seen from Fig. 12, the adsorption rate of the adsorbent on sulfate increased rapidly in the first 90 min, and the rate of increase slowed down from 90 min to 150 min, and the adsorption amount and capacity remained the same after 90 min with further increase in time. This result is because, in the beginning, there are many adsorption sites on the KPC adsorbent, and the free sulfate ions can be adsorbed on the adsorbent quickly.[34] However, with the increased adsorption time, the adsorption gradually reached equilibrium, possibly due to the

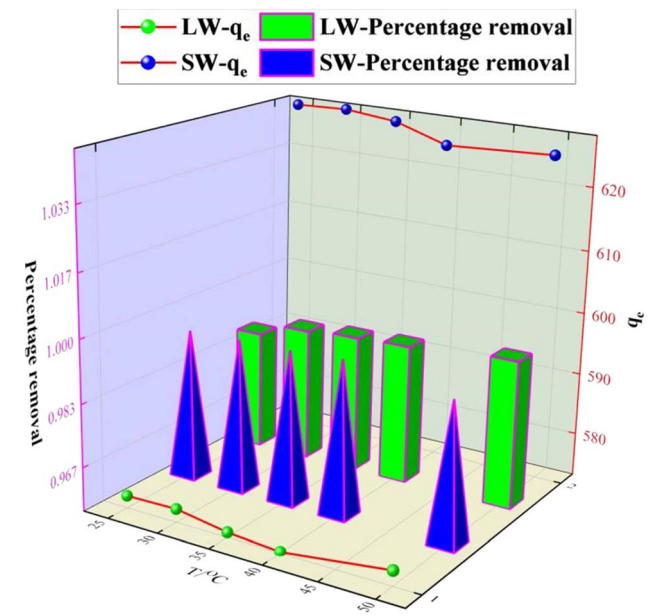

Fig. 10 Effect of temperature on SO_4^{2-} adsorption.

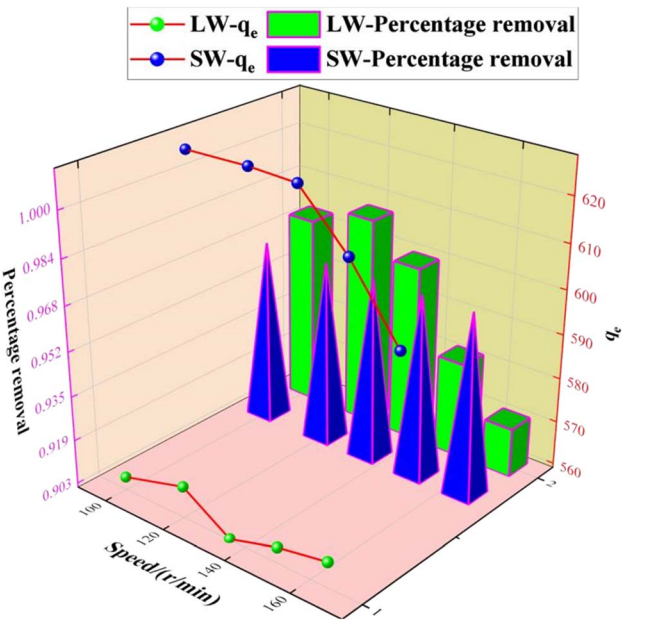

Fig. 11 Effect of the speed rate on SO_4^{2-} adsorption.

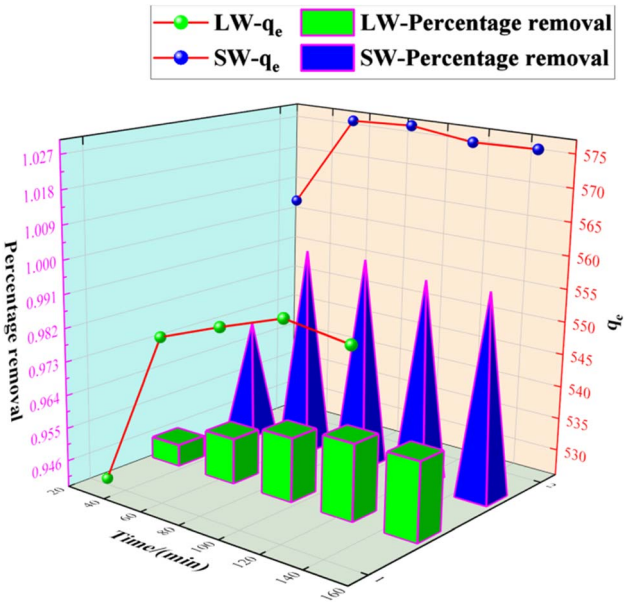

Fig. 12 Effect of contact time on SO_4^{2-} adsorption.

saturation of SO_4^{2-} adsorption after diffusion inside the particles.[2] Therefore, 90 min can be selected as the adsorption equilibrium time, and the adsorption amount reached 557.88 mg g^{-1}.

3.3 Equilibrium adsorption isotherms

The isothermal adsorption model of SO_4^{2-} on KPC was fitted using Langmuir, Freundlich, Langmuir–Freundlich, Temkin, and Dubinin–Radushkevich (D–R) equations, and the fitted curves and parameters are shown in Fig. 13, Table 6 respectively. From the above data results, it can be seen that the fitting effect of KPC isothermal adsorption is Langmuir–Freundlich equation > Langmuir equation > Freundlich equation > D–R equation > Temkin equation. Meanwhile, the correlation coefficient of the Langmuir model ($R^2 = 0.8696$), compared to that of other adsorption models, shows that the KPC adsorption process is more inclined to Langmuir linear fit, indicating that the SO_4^{2-}adsorption process by KPC is dominated by homogeneous adsorption of monomolecular layers and the presence of chemisorption. This result is consistent with reported studies on sulfate adsorption in zirconium oxide-modified biochar.

The theoretical maximum adsorption of KPC at 303.15 K, 313.15 K, and 323.15 K were 793.95 mg g^{-1}, 866.98 mg g^{-1}, and 831.20 mg g^{-1}, respectively, as calculated by using the Langmuir equation, and compared with the experimentally derived 639.44 mg g^{-1}, 691.39 mg g^{-1}, and 647.44 mg g^{-1} from Table 6. At 303.15 K, the KPC adsorption process of SO_4^{2-} was more consistent with the Langmuir fitting model. From Table 6, it can be seen that the R_L value decreases with increasing initial concentration from eqn (5), and the R_L value of the equilibrium constant is between 0 and 1, indicating that adsorption between the adsorbent and the adsorbate is easy. Furthermore, the average free energy of adsorption E for KPC at different temperatures is 5.13 kJ mol^{-1}, 4.88 kJ mol^{-1}, and 5.27 kJ mol^{-1}, respectively, and therefore, is less than 8 kJ mol^{-1}. This result means that the adsorption of SO_4^{2-} from the solution by KPC is physical adsorption.

3.4 Adsorption kinetic study

The kinetic curves and fitted parameters of SO_4^{2-} adsorption on lake water and simulated water are shown in Fig. 14 and Table 7, respectively. The amount of SO_4^{2-} adsorbed by KPC on simulated water is shown. It is evident from the dotted line plot in Fig. 14 that the points of the pseudo-secondary dynamics are basically on the line, indicating that the pseudo-secondary dynamics are relatively well-fitted. From the fitted kinetic data

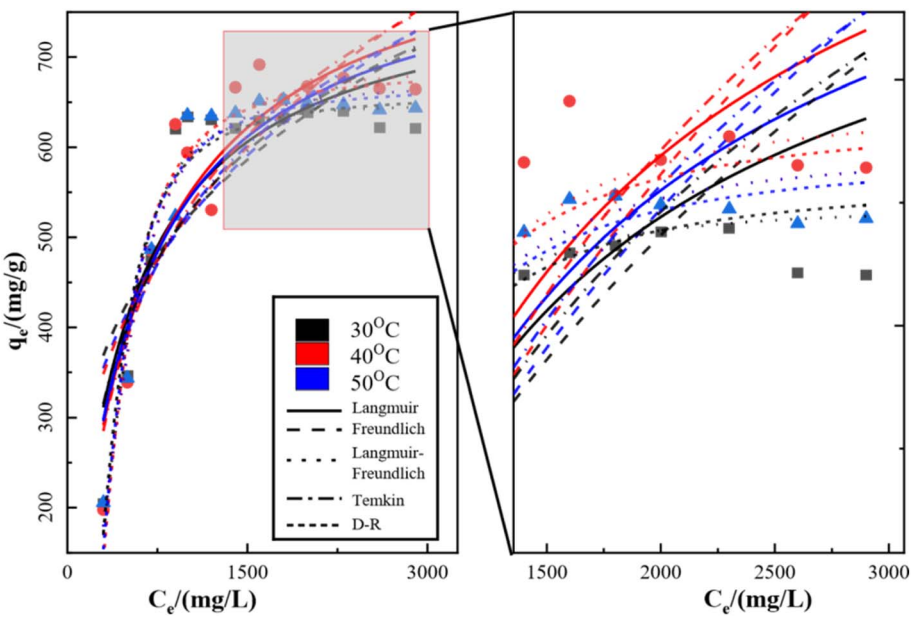

Fig. 13 Isothermal adsorption fitting curve of KPC on SO_4^{2-}.

Table 6 Model parameters of each equation for SO_4^{2-} in simulated water by KPC at different temperatures

	Temperature (K)	Langmuir equation			Freundlich equation		
		q_m (mg g^{-1})	K_L (L mg^{-1})	R^2	K_F (L mg^{-1})	$1/n$	R^2
Non-linear	303.15	793.95	0.00215	0.8118	71.38	0.29	0.6436
	313.15	866.98	0.00169	0.8623	65.31	0.30	0.6807
	323.15	831.20	0.00186	0.8696	57.96	0.32	0.7241

		Langmuir–Freundlich equation			
	T (K)	q_m (mg g^{-1})	KL-F (L mg^{-1})	R^2	n
Non-linear	303.15	647.75	4.37	0.9567	2.79
	313.15	688.48	5.90	0.9424	2.33
	323.15	670.21	3.96	0.9691	2.40

		Temkin equation			D–R equation			
	T (K)	a	b	R^2	q_m (mg g^{-1})	β	R^2	E
Non-linear	303.15	−681.45	174.69	0.7278	655.77	—	0.9398	5.13
	313.15	−875.88	203.57	0.8182	680.76	0.021	0.9269	4.88
	323.15	−789.37	190.30	0.8086	665.98	0.018	0.9513	5.27

in Table 7, it can be seen that the pseudo-secondary kinetic R^2 values are significantly higher than the pseudo-first-order fitted values, which further indicates that the pseudo-secondary kinetic fits are better. Some similar studies were carried out by Gao *et al.*[40], using sugarcane core cellulose-based sorbents to remove SO_4^{2-} in water, which followed a pseudo-secondary kinetic model. Also, by comparing R^2 it can be seen that the fitting effect is Pseudo-second order kinetics > Pseudo-first order kinetics > Elovich. In contrast, KPC reached equilibrium at about 180 min for SO_4^{2-} adsorption in lake water and the adsorption data fit well with the quasi-secondary kinetic model. The theoretical adsorption amount obtained from the quasi-secondary kinetic regression equation is also very close to the experimentally measured adsorption amount, mainly chemisorption. This kinetic model is generally only suitable for describing the kinetic process at the initial adsorption stage. However, it cannot accurately describe the entire process of adsorption, so the SO_4^{2-} adsorption by KPC is consistent with the quasi-secondary kinetic model.

Although the adsorption of SO_4^{2-} in both simulated water and lake water is consistent with the pseudo-first order kinetics, the control step of the reaction rate remains unclear. Nevertheless, our data indicate that the solute diffusion process may control the sulfate adsorption from the surface of the particles to the interior of the particles in solution or by the solute diffusion process from the solution to the surface of the

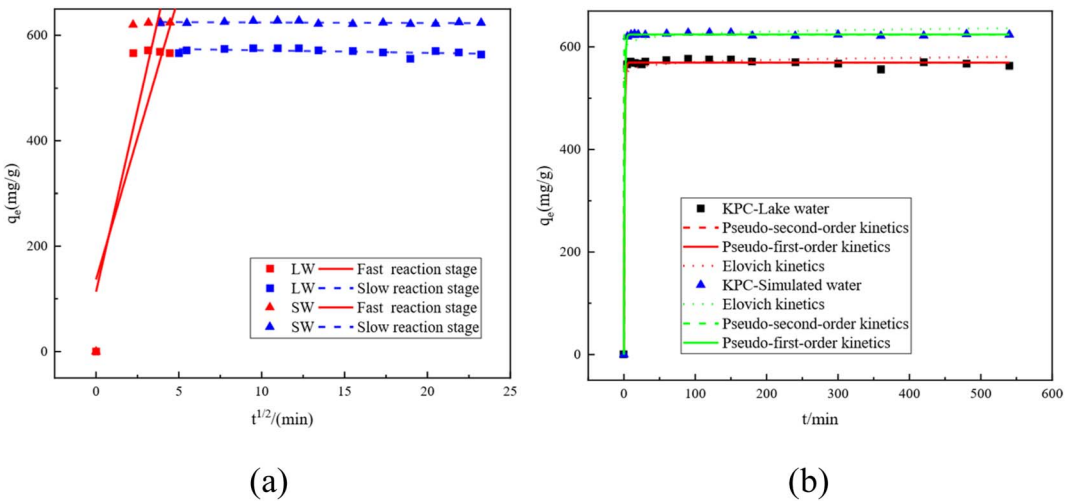

Fig. 14 Fitting curves for the intraparticle diffusion equation of SO_4^{2-} by KPC (a) and kinetic fitting curves (b).

Table 7 Adsorption kinetics and intraparticle diffusion kinetic parameters of KPC for SO_4^{2} adsorption experiments in simulated water and lake water

	Parameter	Kinetics		Kinetics	Fast reaction stage	Slow reaction stage
S W	Parameter 1	$q_e = 624.10$ mg g^{-1}	$q_e = 624.39$ mg g^{-1}	$a = 0.14$	$C = 113.50$	$C = 625.54$
	Parameter 2	$K_1 = 1.0032$ h^{-1}	$K_2 = 0.06$ g (mg h)$^{-1}$	—	$K_3 = 138$, 22 mg (g h$^{1/2}$)$^{-1}$	$K_3 = -0.11$ mg (g h$^{1/2}$)$^{-1}$
	R^2	0.99979	0.9998	0.9951	0.7837	0.0808
L W	Parameter 1	$q_e = 569.23$ mg g^{-1}	$q_e = 569.37$ mg g^{-1}	$a = 0.16$	$C = 136.68$	$C = 576.14$
	Parameter 2	$K_1 = 1.06$ h^{-1}	$K_2 = 0.10$ g (mg h)$^{-1}$	—	$K_3 = 107.63$ mg (g h$^{1/2}$)$^{-1}$	$K_3 = -0.48$ mg (g h$^{1/2}$)$^{-1}$
	R^2	0.9986	0.9987	0.9951	0.7099	0.2063

particles.[41] To determine the actual control steps of the reaction, the experimental data were fitted with the intraparticle diffusion model, and the results are shown in Fig. 14b and Table 7, respectively.

The intra-particle diffusion model can reflect the adsorption mechanism in depth. Fig. 14a shows the kinetic intra-particle diffusion model of sulfate adsorption by KPC. The data show that the whole variation of SO_4^{2-} adsorption by KPC on simulated water can be divided into two linear parts, indicating that the adsorption is divided into two steps.[42,43] The first stage ($t_{1/2} <$ 5.5) is the diffusion of sulfate from the solution phase to the outer surface of the adsorbent, which is a fast adsorption stage and, therefore, a rate control stage. The second stage is the equilibrium stage of sulfate adsorption.

The slope of the SO_4^{2-} adsorption process in simulated water is the largest at $t_{1/2} < 5$, which indicates that the boundary diffusion process is fast and belongs to the fast reaction stage, where the intermolecular interaction forces are mainly electrostatic attraction, dispersion, and hydrogen bonding forces. These forces can make the reaction complete in a very short time. Then, the reaction enters the slow stage, mainly due to the decrease of SO_4^{2} concentration in the solution and the decrease of surface adsorption sites, leading to the decrease of the reaction rate in this stage.[44,45] From the intraparticle diffusion model, if the line passes through the origin, then intraparticle diffusion is the only control step of the rate; if the line does not pass through the origin, then intraparticle diffusion is not the only control step. However, other processes combined with intraparticle diffusion can be responsible for controlling adsorption. Fig. 14a and Table 7 show that the straight line does not pass through the origin, so the adsorption rate of SO_4^{2-} on lake water and simulated water may be controlled by both intraparticle diffusion and surface adsorption.

3.5 Thermodynamic study

The values of b can be obtained from the Langmuir constants K_L and Q_m obtained at different temperatures of 30 °C, 40 °C, and 50 °C. Then we find ΔG^0 based on the linear relationship between nb and ΔG^0, ΔH^0 and ΔS^0. These thermodynamic parameters can be obtained by fitting the linear relationship between ln b and T^{-1}. The results are listed in Table 8.

From the above data, it is clear that the enthalpy change $\Delta H^0 > 0$ is positive, indicating that the adsorption of SO_4^{2-} by KPC is a heat absorption process. The ΔG^0 of the adsorption reaction was negative in the temperature range of 303.15 K–323.15 K. Also, the value appeared to decrease with increasing temperature, indicating that the reaction proceeded spontaneously, which is consistent with the results of previous studies.[46] The Gibbs free energy change ΔG^0 between −20 and 0 kJ mol^{-1} is generally considered physical adsorption, and between −800 and 400 kJ mol^{-1} as chemisorption. However, from the adsorption mechanism, the whole system will be exothermic if the physical adsorption is a single adsorption process. The results indicate that physical adsorption is not the only

Table 8 Values of thermodynamic parameters of sulfate adsorption by KPC

T (K)	b	ΔG^0 (kJ mol^{-1})	ΔH^0 (kJ mol^{-1})	ΔS^0(kJ (mol^{-1} K^{-1}))
303.15	1.71	−14.40	6.47	0.03
313.15	1.47	−16.76	6.47	0.03
323.15	1.55	−19.26	6.47	0.03

Table 9 Maximum adsorption capacity of various materials for sulfate ions

Raw materials	Maximum adsorption (mg g^{-1})	Reference
Coconut shell	4.90	38
Oxide-modified pomelo peel biochar (ZrBC)	35.21	5
PVP-AlNiMn nanocomposite	65.36	39
Fe-modified carbon residue (MCR)	19.50	40
Activated carbon prepared from a *Ziziphus* Spina-Christi lotus leaf	9.30	41
Aluminosilicate modified with uric acid (AA-US)	11.00	42
Ca-doped unmodified chitosan pellets	46.60	43
Barium geo-polymerized blast furnace slag (Ba–BFS-GP)	16.40	44
Pristine & polypyrrole modified UC	44.70	45
Polypyrrole-grafted granular activated carbon	39.06	45
Mg–Fe–CLDHs	111.50	34
Bagasse pith cellulose-based adsorbents (CC/QAC1:1)	500.00	37
KPC	866.98	Current study

adsorption mechanism in the adsorption process of SO_4^{2-} by KPC, and there may be other adsorption mechanisms, such as ion exchange. All of them are negative, and the absolute values of ΔG^0 increase with the increase in temperature, indicating that SO_4^{2-} tends to be adsorbed from the solution to the surface of the adsorbent, and this process is spontaneous.[47] ΔS^0 is positive, and the disorder in the system increases, indicating that entropic push is the driving force for SO_4^{2-} adsorption by KPC, and the disorder at the solid–liquid interface increases during adsorption.

3.6 Comparison of adsorption capacities

The adsorption capacities of several materials for sulfate ions are shown in Table 9. The SO_4^{2-} adsorption capacity by KPC is better than that of any other materials. In addition, this biomass carbon material requires a shorter time to achieve effective sulfate removal.[48] Therefore, KPC has the potential to be an efficient adsorbent for SO_4^{2-} removal.

4 Conclusion

In this study, a new biological carbon material KPC was prepared by the chemical activation method with spent kelp as the raw material and calcium chloride as the activator, and it was used to remove sulfate ions from natural sulfate-rich water and simulated water. The results show that a part of the calcium functional group is loaded in carbon, and a part exists on the surface of KPC in the form of calcium ions. Through the study on the influence of the initial concentration of $SO4^{2-}$, pH, amount of adsorbent and contact time on the adsorption capacity of $SO4^{2-}$ in a simulated water body and lake, the simulated water is more consistent with the Langmuir isothermal equation. The maximum adsorption capacity q_{max} was 866.98 mg g^{-1}. The kinetic studies also show that the simulation and the lake adsorption process conform to the quasi–quadratic reaction model. In addition, the adsorbent also has a high specific surface area and total pore volume, and contains many effective functional groups, which also indicates that KPC has the potential to efficiently remove sulfate ions in wastewater pretreatment. Therefore, the adsorbents prepared based on natural wastes are expected to be used in other fields of wastewater treatment.

Author contributions

Designed and performed the experiments and data analysis: Bingbing Tian. Revised the manuscript: Min Li; Jianjiang Lu; Yanbin Tong. Contributed data analysis and other support: Yalong Song; Rubin Wang; Tianyang Wang; Jinhui Chu; Zhu Qiao and Yi Wang. All authors have read and agreed to the published version of the manuscript.

Conflicts of interest

There are no conflicts to declare.

Acknowledgements

This work was supported by study of the effect of bifunctional surfactants on the structure and photocatalytic activity of $BiVO_4$ (ZZZC202103).

References

1 E.-T. Tolonen, T. Hu, J. Ramo and U. Lassi, *J. Environ. Manage.*, 2016, **181**, 856–862.
2 Q. Li, Y. Li, X. Ma, Q. Du, K. Sui, D. Wang, C. Wang, H. Li and Y. Xia, *Chem. Eng. J.*, 2017, **316**, 623–630.
3 M. Li, C. Dai, B. Yang, Y. Qiao and Z. Zhu, *J. Mater. Eng. Perform.*, 2017, **26**, 764–772.
4 K. K. Kefeni, T. A. M. Msagati and B. B. Mamba, *J. Clean. Prod.*, 2017, **151**, 475–493.
5 H. Ao, W. Cao, Y. Hong, J. Wu and L. Wei, *Sci. Total Environ.*, 2020, 708.
6 I. Kabdasli, A. Bilgin and O. Tunay, *Environ. Technol.*, 2016, **37**, 446–451.
7 V. K. Gupta, I. Ali, T. A. Saleh, A. Nayak and S. Agarwal, *Rsc Adv.*, 2012, **2**, 6380–6388.
8 S. Hong, F. S. Cannon, P. Hou, T. Byrne and C. Nieto-Delgado, *Carbon*, 2014, **73**, 51–60.
9 Q. Xu, W. Li, L. Ma, D. Cao, G. Owens and Z. Chen, *Sci. Total Environ.*, 2020, 703.
10 S. Praveen, J. Jegan, T. B. Pushpa, R. Gokulan and L. Bulgariu, *Biochar*, 2022, 4.
11 T. Ennaert, J. Van Aelst, J. Dijkmans, R. De Clercq, W. Schutyser, M. Dusselier, D. Verboekend and B. F. Sels, *Chem. Soc. Rev.*, 2016, **45**, 584–611.
12 A. Bhatnagar, M. Sillanpaa and A. Witek-Krowiak, *Chem. Eng. J.*, 2015, **270**, 244–271.
13 G. Ohemeng-Boahen, D. D. Sewu and S. H. Woo, *Environ. Sci. Pollut. Res.*, 2019, **26**, 33030–33042.
14 J. Yuan, Y. Zhu, J. Wang, Z. Liu, J. Wu, T. Zhang, P. Li and F. Qiu, *J. Iran. Chem. Soc.*, 2022, **19**, 435–445.
15 D. D. Sewu, P. Boakye, H. Jung and S. H. Woo, *Bioresour. Technol.*, 2017, **244**, 1142–1149.
16 H. Li, X. Ye, Z. Geng, H. Zhou, X. Guo, Y. Zhang, H. Zhao and G. Wang, *J. Hazard. Mater.*, 2016, **304**, 40–48.
17 G. Zhong, H. Xie, Z. Xu, S. Xu, S. Xu, Z. Cai, X. Fu, W. Liao and R. Miao, *Chemistryselect*, 2019, **4**, 3432–3439.
18 S. Bai, T. Wang, Z. Tian, K. Cao and J. Li, *Sci. Rep.*, 2020, 10.
19 N. Popa and M. Visa, *Adv. Powder Technol.*, 2017, **28**, 1866–1876.
20 P. Pengthamkeerati, T. Satapanajaru, N. Chatsatapattayakul, P. Chairattanamanokorn and N. Sananwai, *Desalination*, 2010, **261**, 34–40.
21 P. K. Malik, *Dyes Pigm.*, 2003, **56**, 239–249.
22 M. M. Abd El- Latif and A. M. Ibrahim, *Desalin. Water Treat.*, 2009, DOI: **10.5004/dwt.2009.501**.
23 M. T. Yagub, T. K. Sen and H. M. Ang, *Water Air Soil Pollut.*, 2012, **223**, 5267–5282.
24 S. Li, J. Lyons-Hart, J. Banyasz and K. Shafer, *Fuel*, 2001, **80**, 1809–1817.

25 S. Taghavi, O. Norouzi, A. Tavasoli, F. Di Maria, M. Signoretto, F. Menegazzo and A. Di Michele, *Int. J. Hydrogen Energy*, 2018, **43**, 19918–19929.
26 Y. Zhou, L. Cai, J. Guo, Y. Wang, L. Ji and W. Song, *Appl. Ecol. Environ. Res.*, 2018, **16**, 5837–5847.
27 Y. Wu, Z. Chen, Y. Liu, Y. Xu and Z. Liu, *Fuel*, 2018, **233**, 574–581.
28 K. M. Kwon, I. G. Kim, K.-Y. Lee, H. Kim, M. S. Kim, W. I. Cho, J. Choi and I. W. Nah, *J. Ind. Eng. Chem.*, 2019, **69**, 39–47.
29 A. R. Lucaci, D. Bulgariu, M.-C. Popescu and L. Bulgariu, *Water*, 2020, 12.
30 E.-B. Son, K.-M. Poo, J.-S. Chang and K.-J. Chae, *Sci. Total Environ.*, 2018, **615**, 161–168.
31 X. Yao, L. Ji, J. Guo, S. Ge, W. Lu, Y. Chen, L. Cai, Y. Wang and W. Song, *Bioresour. Technol.*, 2020, 318.
32 X. Yang, T. Kameda, Y. Saito, S. Kumagai and T. Yoshioka, *Inorg. Chem. Commun.*, 2021, 132.
33 Y. Jiang, R. Huang, S. Jiang, Z. Qin and X. Yan, *Int. J. Phytoremediation*, 2018, **20**, 378–383.
34 Z. Kowalczyk, J. Sentek, S. Jodzis, M. Muhler and O. Hinrichsen, *J. Catal.*, 1997, **169**, 407–414.
35 J. Liu, Y. Deng, X. Li and L. Wang, *ACS Sustainable Chem. Eng.*, 2016, **4**, 177–187.
36 A. D. S. V. D. Almeida, W. T. Vieira, M. D. Bispo, S. F. de Melo, T. L. da Silva, T. L. Balliano, M. G. Adeodato Vieira and J. I. Soletti, *J. Environ. Chem.*, 2021, **9**, 104891.
37 J. Liu, X. Yue, Y. Yu and Y. Guo, *Desalin. Water Treat.*, 2015, **56**, 274–283.
38 K.-M. Poo, E.-B. Son, J.-S. Chan, X. Ren, Y.-J. Choi and K.-J. Chae, *J. Environ. Manage.*, 2018, **206**, 364–372.
39 S. Qu, J. Wan, C. Dai, T. Jin and F. Ma, *J. Alloys Compd.*, 2018, **751**, 107–116.
40 X. Gao, H. Zhang, K. Chen, J. Zhou and Q. Liu, *Cellulose*, 2018, **25**, 2531–2545.
41 C. Natnasivayam and D. Sangeetha, *Desalination*, 2008, **219**, 1–13.
42 W. Xin, Y. Song, J. Peng, R. Liu and L. Han, *ACS Sustainable Chem. Eng.*, 2017, **5**, 2312–2319.
43 P. Kinnunen, H. Kyllonen, T. Kaartinen, J. Makinen, J. Heikkinen and V. Miettinen, *Water Sci. Technol.*, 2018, 194–205, DOI: **10.2166/wst.2018.102**.
44 M. Rahmati, G. Yeganeh and H. Esmaeili, *Acta Chim. Slov.*, 2019, **66**, 888–898.
45 A. V. Voronina, M. O. Bajtimirova and V. S. Semenishchev, *J. Radioanal. Nucl. Chem.*, 2022, **331**, 913–920.
46 M. Solgi, L. G. Tabil and L. D. Wilson, *Materials*, 2020, 13.
47 K. Zuo, J. Kim, A. Jain, T. Wang, R. Verduzco, M. Long and Q. Li, *Environ. Sci. Technol.*, 2018, **52**, 9486–9494.
48 S. Hong, F. S. Cannon, P. Hou, T. Byrne and C. Nieto-Delgado, *Chemosphere*, 2017, **184**, 429–437.